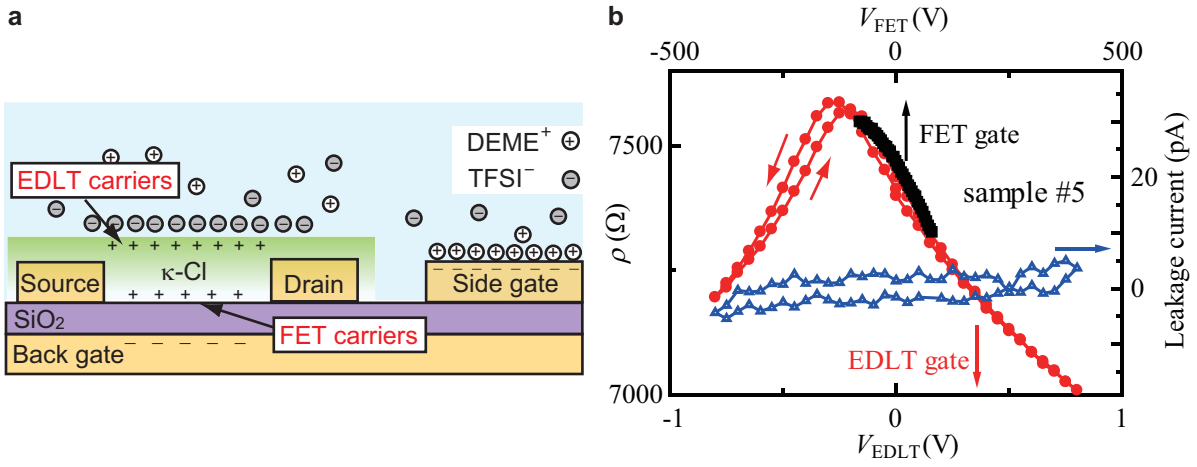


Supplementary Figure 1. **Comparison experiment between FET and EDLT devices using the same $\kappa$-Cl crystal.** **a,** Schematic side view of the FET and EDLT devices. **b**, Transfer curves of sample #5 at 220 K. The gate voltage dependence of the resistivity for the FET (black square) and EDLT operations (red circle) are shown. Blue triangle denotes the leakage current for the EDLT operation.

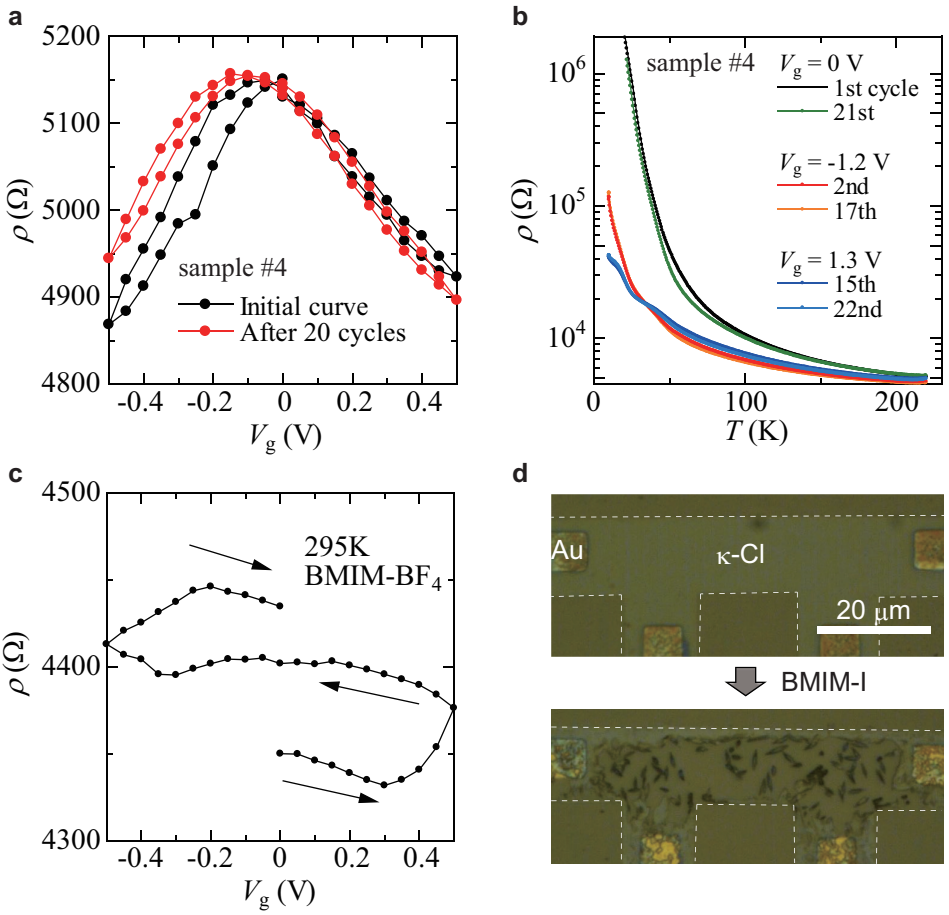


Supplementary Figure 2. **Repeatability of the measurements. a,** Gate voltage dependence of the sheet resistivity at 220 K before and after 20 temperature cycles. **b**, Temperature dependence of the sheet resistivity during the 1st, 21st, 2nd, 17th, 15th and 22nd temperature cycles. **c**, Gate voltage dependence of the sheet resistivity at 295 K. **d**, Optical image of a laser-shaped $\kappa$-Cl crystal before and after the drop of BMIM-I. The white broken lines denote the shape of the crystal. The sample was immediately rinsed with 2-propanol a few seconds after the drop.

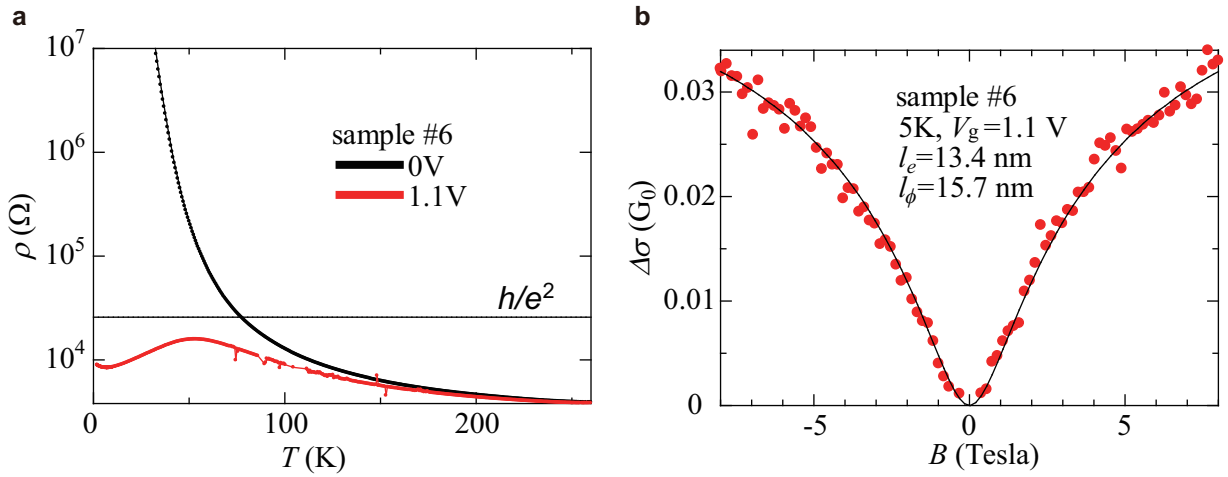


Supplementary Figure 3. **Negative magnetoresistance under electron doping.** **a,** Temperature dependences of the sheet resistivity in sample #6 at $V_g = 0$ and +1.1 V. **b**, Negative magnetoresistance at 5 K, $V_g = +1.1$ V where $G_0 = 2e^2/h$ and least-squares fitting with the digamma functions (Supplementary Eq.(1)).

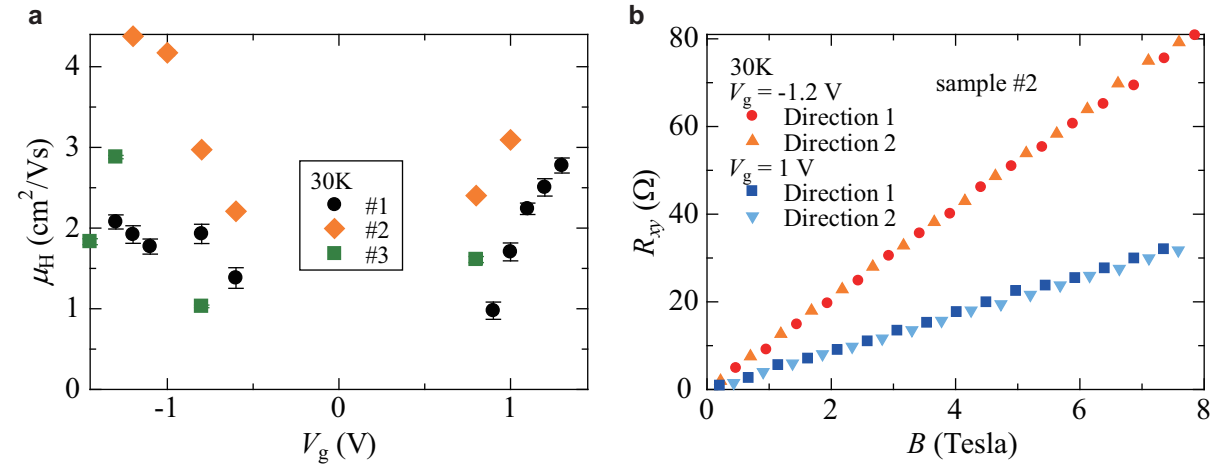


Supplementary Figure 4. **Hall mobility.** **a,** Gate voltage dependence of the Hall mobility at 30 K. The error bars were calculated from the standard deviation of the Hall resistance vs magnetic field plots. **b**, Hall resistance vs magnetic field with two mutually-perpendicular current directions at 30 K. The directions 1 and 2 are parallel to the diagonals of the crystal, namely, *a*- or *c*-axis.

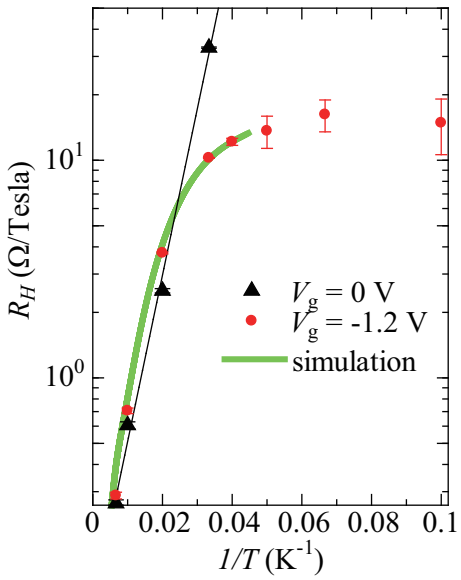


Supplementary Figure 5. **Temperature dependence of the measured and simulated Hall coefficient.** Black triangle and red circle denote the measured $R_{\rm H}$ at $V_{\rm g} = 0$ and $-1.2$ V, respectively. The measured $R_{\rm H}$ and the errors are taken from Fig. 3b in the main text. Green thick line is a simulation of $R_{\rm H}$ at $V_{\rm g} = -1.2$ V by Supplementary Eq. (2). It is reproduced by the constant $R_{\rm Hs}$ and thermally excited $R_{\rm Hb}$ (black thin line) down to approximately 22 K. At lower temperature, the simulation is not applicable because $\sigma_{\rm b}$ is not measurable.

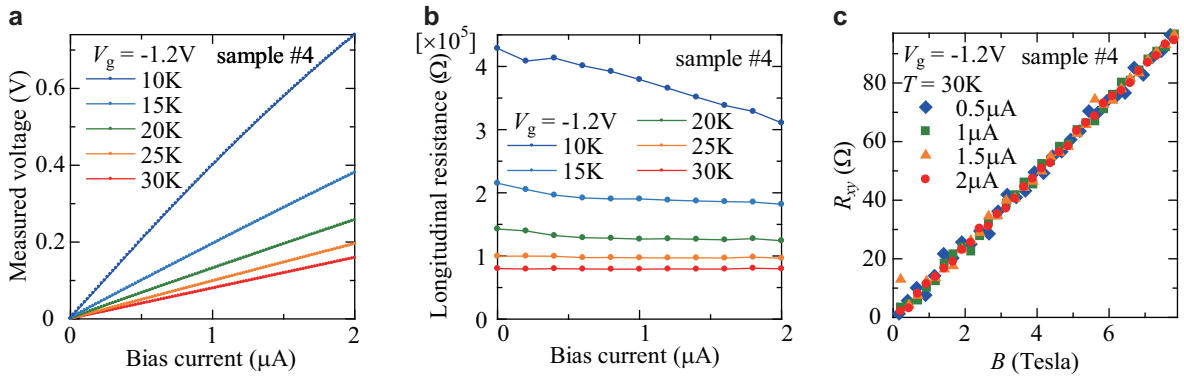


Supplementary Figure 6. **Current-voltage characteristics. a,b,** Current-voltage characteristics (**a**) and current dependence of the longitudinal resistance (**b**) at $V_{\rm g} = -1.2$ V and $T = 10$, 15, 20, 25 and 30 K. **c**, Hall resistance vs magnetic field under various applied current at 30 K.

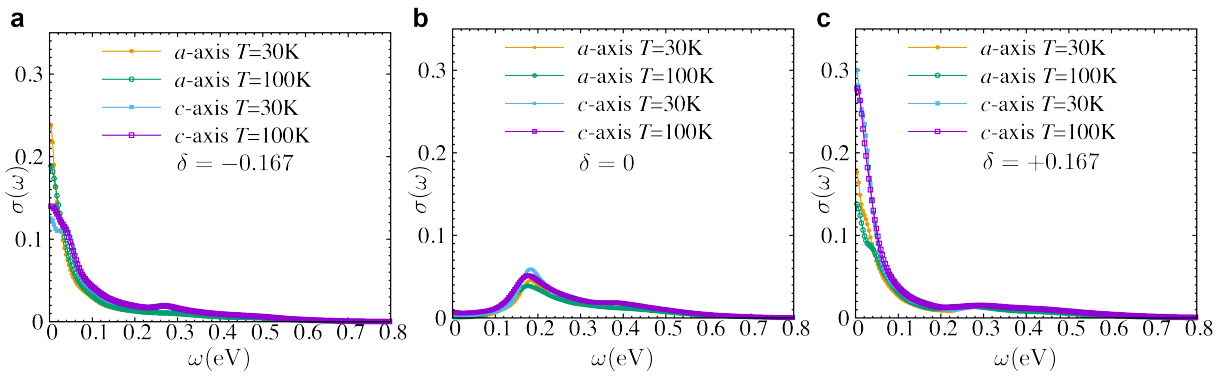


Supplementary Figure 7. **Optical conductivity.** The temperature dependence of the optical conductivity along the $a$- and $c$-axes for **a,** hole-doped ($\delta = -0.167$), **b,** half-filled ($\delta = 0$) and **c,** electron-doped ($\delta = 0.167$) cases.

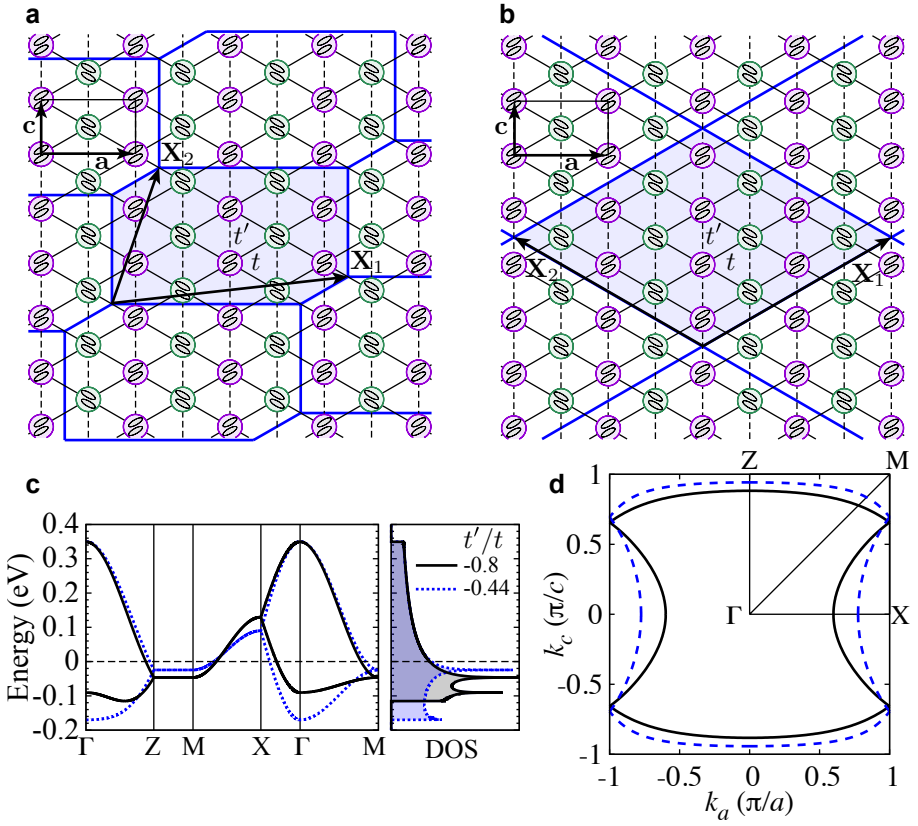


Supplementary Figure 8. **The clusters used in the CPT calculations and electronic structures in the non-interacting limit. a,** A schematic of the BEDT-TTF layer ($a$-$c$ plane) of $\kappa$-type BEDT-TTF salts described by the Hubbard model on the anisotropic triangular lattice with transfer integrals $t$ (solid lines) and $t'$ (thin dashed lines). The single site consists of a single BEDT-TTF dimer. Different orientation of dimers represents the crystallographically different dimers. A unit cell and primitive translational vectors $\mathbf{a} = (a, 0)$ and $\mathbf{c} = (0, c)$ are indicated as a solid rectangle and solid arrows, respectively. The translational vectors $\mathbf{X}_1$ and $\mathbf{X}_2$ for the 12-site cluster (shaded area) are also denoted as thick solid arrows. The blue solid lines represent the partitioning of the triangular lattice into the 12-site clusters for the CPT calculations. **b,** Same as **a** but for the partitioning into the 16-site clusters. **c,** The non-interacting tight-binding band structure (left) and the density of states (right) with $t'/t = -0.8$ and $t = 55$ meV (solid lines). For comparison, the results with $t'/t = -0.44$ and $t = 65$ meV are also shown by dashed lines. The horizontal lines indicate the Fermi energy at half filling. Here, $\Gamma = (0, 0)$, Z$= (0, \pi/c)$, M$= (\pi/a, \pi/c)$, and X$= (\pi/a, 0)$. **d,** The Fermi surfaces for the non-interacting case with $t'/t = -0.8$ (solid lines) and $t'/t = -0.44$ (dashed lines) at half filling.

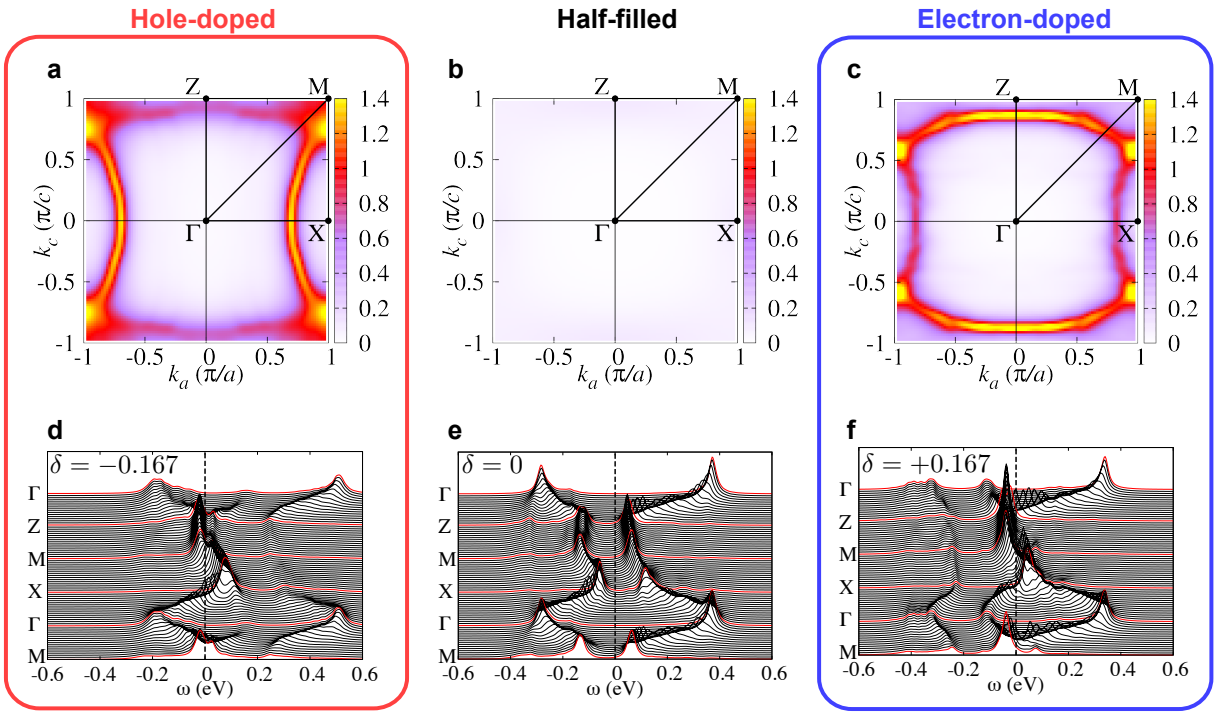


Supplementary Figure 9. **Fermi surfaces and the single-particle spectral functions of the Hubbard model on an anisotropic triangular lattice at 30 K. a,b,c,** Fermi surfaces in the 1st BZ of $\kappa$-Cl for 17% hole doping **(a)**, half filling **(b)** and 17% electron doping **(c)**, determined by the largest spectral intensity at the Fermi energy. **d,e,f,** Single-particle spectral functions for 17% hole doping **(d)**, half filling **(e)** and 17% electron doping **(f)**. The Fermi energy is located at $\omega = 0$ and the parameter set of this model is $t'/t = -0.44$, $U/t = 5.5$ and $t = 65$ meV.

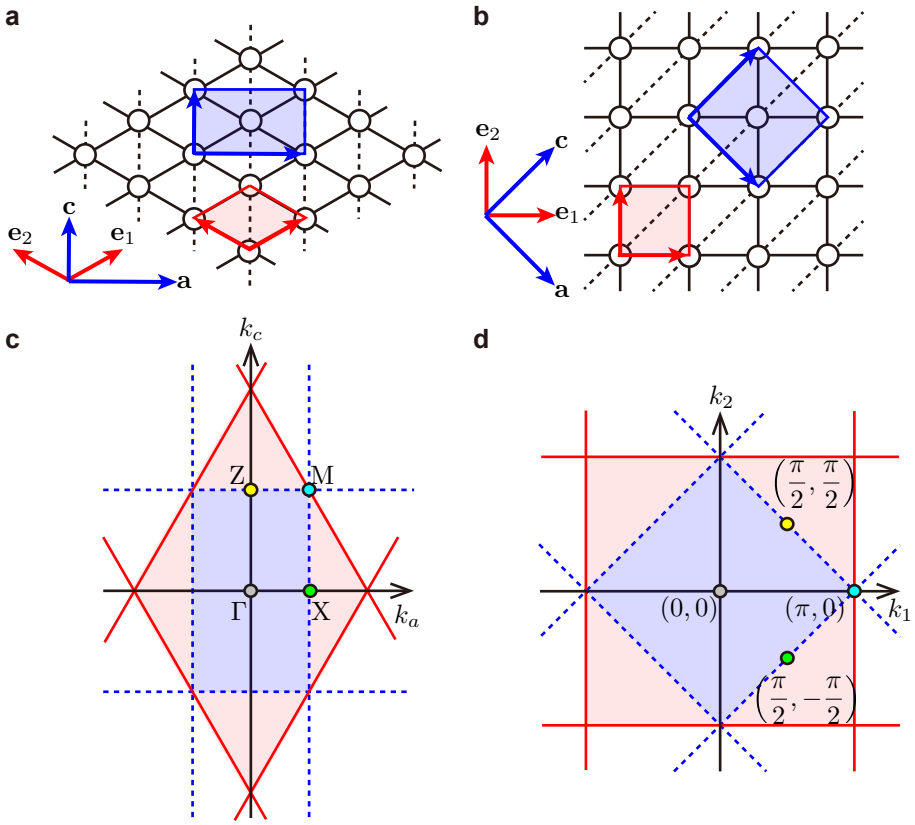


Supplementary Figure 10. **Unit cells and Brillouin zones.** **a,** The anisotropic triangular lattice. The translational vectors $\mathbf{e}_1$ and $\mathbf{e}_2$ (**a** and **c**) are represented by the red (blue) arrows. The red (blue) shaded region represents the unit cell containing one site (two sites). **b,** The lattice topologically equivalent to that in **a**. Notice that $\mathbf{a} = \mathbf{e}_1 - \mathbf{e}_2$ and $\mathbf{c} = \mathbf{e}_1 + \mathbf{e}_2$ in both figures **a** and **b**. **c,** The momentum space for the anisotropic triangular lattice in **a**. The BZ of the one-(two)-site unit cell is represented by the red (blue) shaded region bounded by the red solid (blue dashed) lines. **d,** The same as **c** but for the lattice in **b**.

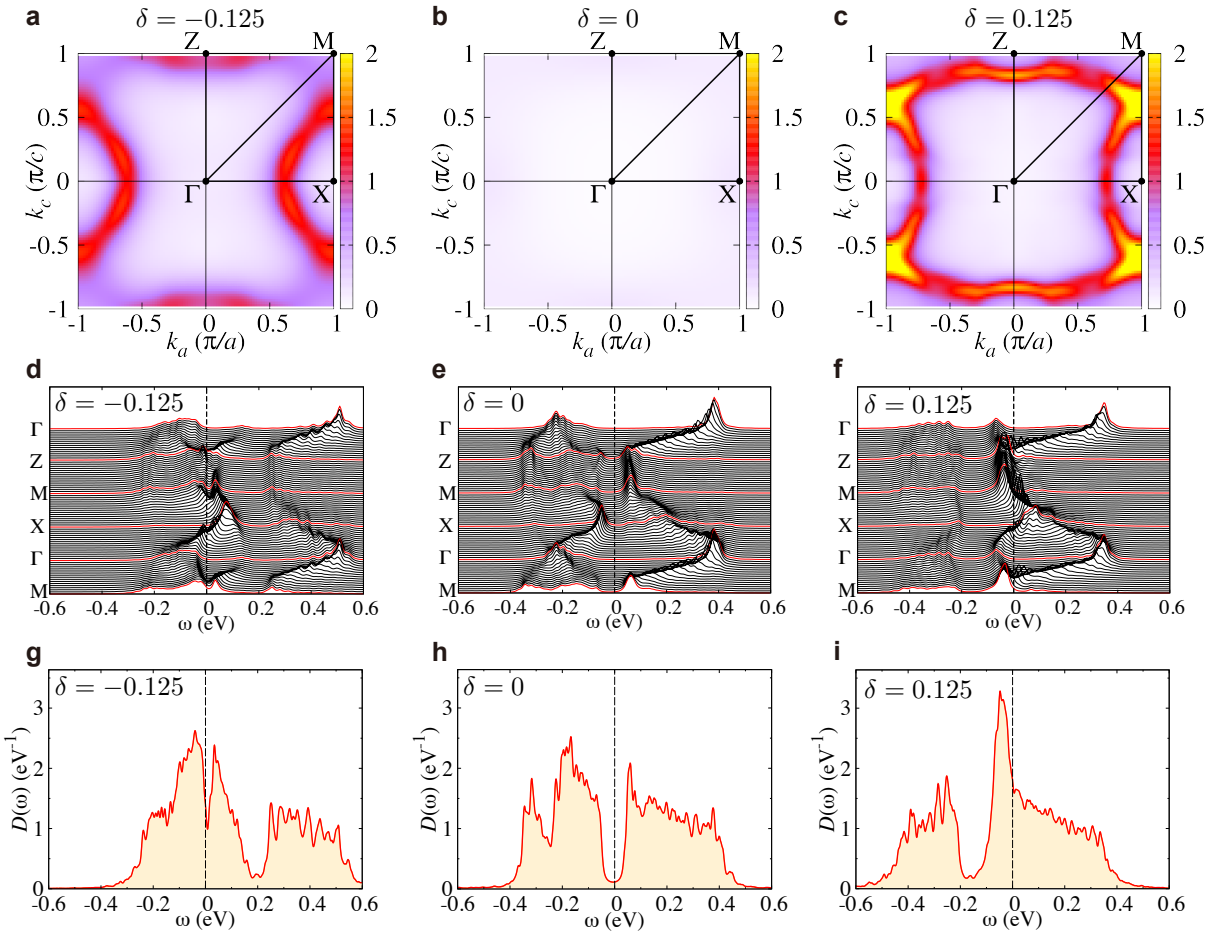


Supplementary Figure 11. **Fermi surfaces, single-particle excitations, and density of states of the single-band Hubbard model on an anisotropic triangular lattice at 0 K with the 16-site cluster.** **a, b, c,** The Fermi surfaces, **d, e, f,** the single-particle spectral functions and **g, h, i,** the density of states for hole-doped (**a, d, g**), half-filled (**b, e, h**) and electron-doped (**c, f, i**) cases. $\delta$ indicates the electron doping per dimer. The Fermi energy is indicated as vertical dashed lines in d-i.

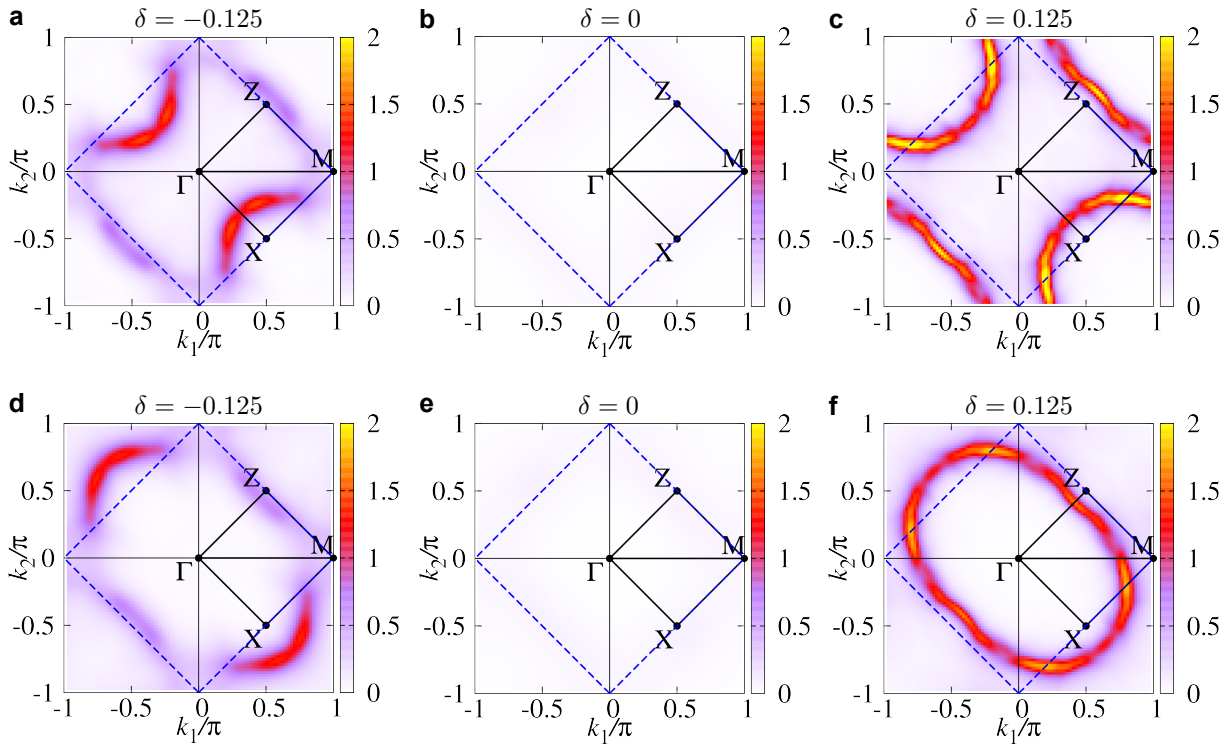


Supplementary Figure 12. **The Fermi surfaces in unfolded Brillouin zones at 0 K with the 16-site cluster. a, b, c,** The Fermi surface at electron doping per dimer $\delta = -0.125$ (**a**), $\delta = 0$ (**b**), and $\delta = 0.125$ (**c**) shown in an "unfolded" BZ. **d, e, f,** Same as the top panels but for a different "unfolded" BZ centered at the Γ point of the second BZ. The wave vectors $k_1$ and $k_2$ are defined by Eq.(3) in the Methods section. The blue dashed lines represent the boundaries of the BZ.

**Supplementary Note 1: Comparison experiment between the FET and EDLT devices using the same $\kappa$-Cl crystal**

To check the carrier tunability of the electric double layer on $\kappa$-Cl, we compared the field effect of the EDLT (DEME-TFSI gate) and FET ($SiO_2$ gate) in the same $\kappa$-Cl crystal at 220 K (sample #5, Supplementary Fig. 1). Using the $SiO_2$ gate, we observed n-type FET behavior with a field-effect mobility of 2.6 $cm^2/Vs$. On the other hand, a clear ambipolar field effect with a resistance peak at approximately $-0.25$ V was observed for the DEME-TFSI gate. The hysteresis and the leakage current remained small without any signature of a chemical reaction between the electrolyte and $\kappa$-Cl. As shown in Supplementary Fig. 1, the resistivity curves for the FET and EDLT almost coincide when we adjust the gate voltage axis. Provided that the mobilities of the FET and EDLT are equivalent, the capacitance of the electric double layer on the electron-doping side is about 500 times larger than that of the FET. As a result, gate voltage of +1 V in the EDLT corresponded to approximately 20% electron doping ($3.6\times10^{13}$ $cm^{-2}$).

As shown in Fig. 3c, the Hall coefficient at $V_g = +1$ V in sample #2 (which shows the smallest error) gives a hole density of $1.47\times10^{14}$ $cm^{-2}$ at 30 K. Using the half-filled hole density of $\kappa$-Cl, $1.86\times10^{14}$ $cm^{-2}$, the density of injected electrons is estimated as $0.39\times10^{14}$ $cm^{-2}$ ($= 1.86\times10^{14}$ $cm^{-2}-1.47\times10^{14}$ $cm^{-2}$), which corresponds to 21% electron doping. This value coincides the above estimate of 20% within 1% error. However, as stated in Supplementary Note 5, the experimental carrier density contains influences of thermally excited carriers in the bulk, and the absolute value of the above estimate of 20% is not as accurate as it appears. Despite these complications, the relative trend of the carrier density should be reliable enough to support the discussions in the main text, because similar amount of errors in the same direction (or baseline shift) should be included for all the measured data.

**Supplementary Note 2: Repeatability after low temperature measurements**

We checked the effect of multiple temperature cycles together with the gate voltage application, on the transfer curve at 220 K and the temperature dependence of the resistivity in sample #4. The applied gate voltage in each temperature cycle (between 220 and 10 K)

was as follows: 0, −1.2, −1, −0.8, −0.6, −0.4, −0.2, 0, 0.2, 0.4, 0.6, 0.8, 1, 1.2, 1.3 1.4, −1.2, −1.3, 0, 1.3, 0, 1.3 and 1.35 V. As shown in Supplementary Fig. 2a, the transfer curve at 220 K was reproducible after 20 temperature cycles despite the slight shift of approximately 0.1 V to the hole-doped side. The temperature dependence of the resistivity (Supplementary Fig. 2b) was also reproducible after multiple temperature cycles with the gate voltage application of ±1.3 V. Therefore, it is unlikely that the sample is mechanically damaged due to thermal stress or degraded by destructive chemical reaction between the sample and gate electrolyte.

On the other hand, when we applied gate voltage at room temperature, the resistance irreversibly increased at $|V_g| > 0.3$ V (Supplementary Fig. 2c). Moreover, when we dropped 1-butyl-3-methylimidazolium iodide (BMIM-I) on $\kappa$-Cl, the crystal was immediately dissolved without gate voltage as shown in Supplementary Fig. 2d. Thus, although our device is weak against gate voltage application at room temperature and/or ionic liquids with large oxidizability, appropriate choice of ionic liquid and temperature enables repeatable measurements.

**Supplementary Note 3: Negative magnetoresistance in a metallic sample under electron doping**

In a high-conductivity sample (sample #6), we observed negative magnetoresistance at 5 K which is the hallmark of the weak localisation effect. As shown in Supplementary Fig. 3, the negative magnetoresistance was fitted with the formula [1]

$$\Delta\sigma = -\frac{e^2}{\pi h}\left[\psi\left(\frac{1}{2}+\frac{\hbar}{4eBl_e^2}\right)-\psi\left(\frac{1}{2}+\frac{\hbar}{4eBl_\phi^2}\right)-2\ln\frac{l_\phi}{l_e}\right] \quad (1)$$

where $\psi$ denotes the digamma function, and $\Delta\sigma$, $B$, $l_e$ and $l_\phi$ are deviation of the sheet conductivity from that under zero magnetic field, the applied magnetic flux density, mean free path and dephasing length of the carriers, respectively. $l_e$ and $l_\phi$ were estimated to be 13.4 nm and 15.7 nm from the least-squares fitting. These values considerably exceed the distance between BEDT-TTF dimers (∼1 nm) indicating coherent transport, in contrast to the Mott insulating state.

**Supplementary Note 4: Gate voltage dependence of the Hall mobility**

The Hall mobility $\mu_{\rm H}$ is given by the product of the Hall coefficient and the conductivity. Supplementary Figure 4a shows the gate voltage dependence of the Hall mobility in sample #1−3 at 30 K. The results have two implications: First, the Hall mobility is more sample-dependent than the Hall coefficient (Fig. 3c in the main text). Namely, the mobility is highly sample dependent due to the surface conditions such as roughness, while the carrier density under gate voltage is more robust. Second, the Hall mobilities are comparable between the hole- and electron-doped states, although the data contain ambiguities owing to the conductivity anisotropy (on the other hand, the Hall effect is isotropic as shown in Supplementary Fig. 4b). This does not contradict to our calculations because the suppressed spectral function near the Z-M line under hole doping do not predominantly contribute to the Hall coefficient and conductivity. Therefore, the difference of electron correlation effects between the electron- and hole-doped states cannot be examined via the Hall mobility in the present study.

**Supplementary Note 5: Influence of thermally excited carriers on the Hall coefficient**

Since the samples consist of several tens of conducting BEDT-TTF layers, the $R_{\rm H}$ values more or less contain information of thermally excited carriers in the bulk. Here, we show that the presence of thermally excited carriers in the bulk explains the temperature dependence of $R_{\rm H}$ (Fig. 3b). For sample #2, we can roughly estimate the value at the surface (at $T$ = 30 K and $V_{\rm g}$ = −1.2 V) on the assumption that $R_{\rm H}$ at $T$ = 30 K and $V_{\rm g}$ = 0 V purely originates from the bulk. When two types of hole carriers (for bulk and surface) coexist, the Hall coefficient $R_{\rm H}$ is expressed as

$$R_{\rm H} = \frac{\mu_{\rm b}^2 n_{\rm b} + \mu_{\rm s}^2 n_{\rm s}}{e(\mu_{\rm s} n_{\rm s} + \mu_{\rm s} n_{\rm s})^2} = \frac{R_{\rm Hb}\sigma_{\rm b}^2 + R_{\rm Hs}\sigma_{\rm s}^2}{\sigma^2} \tag{2}$$

where $\mu_{\rm b/s}$, $n_{\rm b/s}$, $\sigma_{\rm b/s} = e\mu_{\rm b/s} n_{\rm b/s}$, and $R_{\rm Hb/s} = 1/en_{\rm b/s}$ denote the mobility, carrier density, conductivity, and Hall coefficient for the bulk/surface, respectively, and $\sigma = \sigma_{\rm b} + \sigma_{\rm s}$. The surface Hall coefficient $R_{\rm Hs}$ is therefore estimated from

$$R_{\rm Hs} = \frac{R_{\rm H}\sigma^2 - R_{\rm Hb}\sigma_{\rm b}^2}{\sigma_{\rm s}^2}. \tag{3}$$

By substituting measured values ($R_{\rm H} = 10.25$ Ω/Tesla, $R_{\rm Hb} = 32.92$ Ω/Tesla, $\sigma = 43.40$ μS, $\sigma_{\rm b} = 8.56$ μS and $\sigma_{\rm s} = 34.84$ μS) at 30 K on the right-hand side of Supplementary Eq. (3), we obtain $R_{\rm Hs} = 13.9$ Ω/Tesla at $T = 30$ K and $V_{\rm g} = -1.2$ V. Although this value contains ambiguity owing to the resistivity anisotropy, the value is close to that at 20 K (13.64 Ω/Tesla) and within the error bars of $R_{\rm H}$ at lower temperatures including $T = 20$, 15 and 10 K. The errors are calculated from the standard deviation of the $R_{xy}$ vs magnetic field plots and the ambiguity originating from the non-ohmic behaviour at low temperature (see Supplementary Note 6). Thus, the true value of $R_{\rm Hs}$ at 30 K is probably close to the measured $R_{\rm H}$ at 20 K, but the data below 30 K also contain non-ohmicity. We therefore used the data at 30 K in Fig. 3. Although we have such multiple origins of the errors on $R_{\rm H}$ value, the general trend of $R_{\rm H}$ vs $V_{\rm g}$ plot in the main text should not be as uncertain as the errors indicate, because those errors do not cause a random scattering but cause baseline shift which preserve the relative values between data points. Thus we believe that the $R_{\rm H}$ data are well representing the surface states and support our claims in the main text.

Having estimated the surface Hall coefficient $R_{\rm Hs}$ at 30 K, we then simulated the temperature dependence of the total Hall coefficient $R_{\rm H}$ at $V_{\rm g} = -1.2$ V with the two-carrier model in Supplementary Eq. (2), by assuming constant surface Hall coefficient $R_{\rm Hs} = 13.9$ Ω/Tesla and thermally excited bulk Hall coefficient $R_{\rm Hb} = 8.78 \times 10^{-2} \times \exp\left(E_{\rm a}/k_{\rm B}T\right)$ Ω/Tesla with $E_{\rm a}/k_{\rm B} = 176$ K (black thin line in Supplementary Fig. 5). The experimentally measured values are also used for the temperature dependence of $\sigma$, $\sigma_{\rm b}$, and $\sigma_{\rm s}$ in Supplementary Eq. (2). Notice that the simulation is not applicable for the temperatures lower than approximately 22 K because $\sigma_{\rm b}$ is not measurable. As shown in Supplementary Fig. 5, the measured values of $R_{\rm H}$ (red circle) are reproduced by this simple two-carrier model with constant surface Hall coefficient $R_{\rm Hs}$ and thermally excited bulk Hall coefficient $R_{\rm Hb}$ (green thick line). The increase in $R_{\rm H}$ upon cooling has been thus described by considering the influence of thermally excited carriers in the bulk.

**Supplementary Note 6: Current-voltage characteristics in the insulating state under hole doping**

Since the hole-doped samples remained insulating, we measured the current-voltage characteristics at low temperature to test the ohmicity of the conduction. Supplementary Fig-

ures 6a and b show the current-voltage characteristics and the current dependence of the longitudinal resistance at $V_{\rm g} = -1.2$ V and $T = 10$, 15, 20, 25 and 30 K. The current-voltage characteristics were non-ohmic below 20 K, whereas the longitudinal and Hall resistances did not depend on the applied current at 30 K (Supplementary Fig. 6b and c).

The error bars in Fig. 3b are calculated by taking into account the standard deviation $s$ of the $R_{xy}$ vs magnetic field plots and the ambiguity $\alpha$ originating from the non-ohmic behaviour. Since we applied 1 $\mu$A for the Hall measurements, $\alpha$ was defined as $\alpha = (R_{0\rm A} - R_{1\mu\rm A})/R_{1\mu\rm A}$ at each temperature, where $R_{0\rm A}$ and $R_{1\mu\rm A}$ denote the resistances at 0 A and 1 $\mu$A in Supplementary Fig. 4b. The error bars in Fig. 3b were estimated from $(1+\alpha)(R_{\rm H}+s)-R_{\rm H}$ (here, $R_{\rm H}$ is the most probable value).

**Supplementary Note 7: Optical conductivity**

As described in the main text, we have observed experimentally that the electric resistivity exhibits anisotropy in particular for the hole-doped case at low temperature ($T \sim 30$ K), and the anisotropy is gradually weakened with increasing the temperature. Here, we calculate the optical conductivity along $a$- and $c$-axes and show that they indeed exhibits the anisotropy and the temperature dependence consistent with the experiments.

The optical conductivity along $a$ ($c$) direction is defined as

$$\sigma_{a/c}(\omega) = \frac{\pi}{V_{\rm BZ}} \int_{\rm BZ} {\rm d}\mathbf{k} \int {\rm d}\omega' \frac{f(\omega'-\omega) - f(\omega')}{\omega} A(\mathbf{k}, \omega'-\omega) A(\mathbf{k}, \omega') v^2_{\mathbf{k}a/c}, \tag{4}$$

where $f(\omega) = ({\rm e}^{\omega/T}+1)^{-1}$ is the Fermi distribution function,

$$v_{\mathbf{k},a} = t \sin k_1 - t \sin k_2 \tag{5}$$

is the velocity of the non-interacting electrons along $a$-axis, and

$$v_{\mathbf{k},c} = t \sin k_1 + t \sin k_2 + 2t' \sin(k_1 + k_2) \tag{6}$$

is that along $c$-axis. Notice that the optical conductivity in Supplementary Eq. (4) does not include the vertex corrections. Supplementary Figures 7**a**, **b**, and **c** show the temperature dependence of the optical conductivity along the $a$- and $c$-axes for hole-doped, half-filled, and electron-doped cases, respectively. Here we use the parameter set of $t'/t = -0.44$, $U/t = 5.5$, and $t = 65$ meV.

At half filling, a broad peak appears at $\omega \sim 0.18$ eV. This peak corresponds to the excitation from the lower Hubbard band to the upper Hubbard band. Although the peak is slightly broadened when the temperature is increased, its position and overall structure are almost independent of the temperature since the energy scale of the electron interaction $U \simeq 0.36$ eV $\simeq 4200$ K is much larger than that of the temperature considered. In the doped cases, the peak at $\omega \sim 0.18$ eV found at half filling disappears while a shoulder remains at $\omega \sim 0.25$ eV. This spectral-weight transfer is the characteristic feature of the doped Mott insulators [2] also observed in the cuprate high-temperature superconductor [3].

As shown in Supplementary Fig. 7**b**, the anisotropy is weak at half filling. This is because the high-energy excitations across the Mott gap originates in the local electronic states, and therefore it is insensitive to the direction. When the carriers are doped, the zero-energy excitations become possible and the anisotropy is clearly observed in the low-energy region ($\omega \lesssim 0.05$ eV). For the hole doped case (Supplementary Fig. 7**a**), $\sigma_a(\omega)$ is twice as large as $\sigma_c(\omega)$ at $T = 30$ K in the low-energy limit, but the anisotropy becomes weaker when the temperature is increased to $T = 100$ K. For the electron doped case at $T = 30$ K, the anisotropy is smaller than that in the hole-doped case. However, as shown in Supplementary Fig. 7**c**, the anisotropy is reversed under the electron doping. This is in good accordance with the resistivity measurement under the electron doping at low temperatures. We have thus shown that the low-energy excitations in the optical conductivity exhibit significant spatial anisotropy and temperature dependence, which is in good qualitative agreement with the resistivity experiment.

**Supplementary Note 8: Additional results at zero temperature with the 16-site cluster**

Supplementary Figure 11 summarizes the results of the 16-site cluster with $t'/t = -0.8$, $U/t = 7$, and $t = 55$ meV calculated at zero temperature. The electron-hole asymmetry of the Fermi surface can be seen clearly in Supplementary Fig. 11a-c. The single-particle spectral functions in Supplementary Fig. 11d-f exhibit qualitatively the same results with those of the 12-site cluster shown in the main text. Supplementary Fig. 11g-i show the density of states

$$D(\omega) = \frac{1}{V_{\mathrm{BZ}}} \int_{\mathrm{BZ}} \mathrm{d}\mathbf{k} A(\mathbf{k}, \omega), \tag{7}$$

where $V_{\rm BZ} = (2\pi)^2/(ac)$ is the volume of the BZ and the integration over $\mathbf{k}$ is taken in the BZ. The substantial suppression of the density of states at the Fermi energy, i.e., the pseudogap, is observed in the hole-doped case (see Supplementary Fig. 11g), consistent with the observation of the Fermi arc. On the other hand, such suppression of the density of states at the Fermi energy is hardly seen in the electron doped case (see Supplementary Fig. 11i). These results demonstrate that the electron-hole asymmetry is not affected by the clusters chosen for the CPT calculations.

Finally, we show the Fermi surfaces in "unfolded" BZ in Supplementary Fig. 12. These plots are easily compared with other theoretical calculations often performed on the triangular lattice with the single-site unit cell [4]. Supplementary Fig. 12a-c show the Fermi surface calculated with the 16-site cluster at zero temperature. Here the unfolded BZ is centred at $\Gamma$ point of the first BZ of the triangular lattice with the two-site unit cell. Supplementary Fig. 12d-f are the same as panels a-c, but the unfolded BZ is centered at $\Gamma$ point of one of the second BZs. In both plots, one can again observe clearly the electron-hole asymmetric reconstruction of the Fermi surface.

---


[1] Nagaoka, Y. Theory of Anderson localization. *Progr. Theoret. Phys. Suppl.* **84**, 1-15 (1985).

[2] Eskes, H., Oleś, A. M., Meinders, M. B. J. & Stephan, W. Spectral properties of the Hubbard bands. *Phys. Rev. B* **50**, 17980-18002 (1994).

[3] Uchida, S. Ido, T., Takagi, H., Arima, T., Tokura, Y. & Tajima, S. Optical spectra of $La_{2-x}Sr_xCuO_4$: Effect of carrier doping on the electronic structure of the $CuO_2$ plane. *Phys. Rev. B* **43**, 7942-7954 (1991).

[4] Kang, J., Yu, S.-L., Xiang, T. & Li, J.-X. Pseudogap and Fermi arc in $\kappa$-type organic superconductors. *Phys. Rev. B* **84**, 064520 (2011).